



# Mesoporous supported cobalt catalysts for enhanced hydrogen production during cellulose decomposition

Ming Zhao<sup>a</sup>, Nicholas H. Florin<sup>b</sup>, Andrew T. Harris<sup>a,\*</sup>

<sup>a</sup> Laboratory for Sustainable Technology, School of Chemical and Biomolecular Engineering, The University of Sydney, NSW, 2006, Australia

<sup>b</sup> Grantham Institute for Climate Change, The Imperial College, South Kensington Campus, London SW7 2AZ, United Kingdom

## ARTICLE INFO

### Article history:

Received 23 December 2009

Received in revised form 25 March 2010

Accepted 25 March 2010

Available online 1 April 2010

### Keywords:

Hydrogen

H<sub>2</sub> production

Cellulose

Mesoporous

Supported Co catalyst

TG-MS

## ABSTRACT

Two groups of cobalt (Co) catalysts, supported on SBA-15 and MCM-41, respectively, were prepared by incipient wetness impregnation and tested for their influence on the thermal decomposition of acetyl cellulose.  $\gamma$ -Al<sub>2</sub>O<sub>3</sub> supported Co catalysts were investigated as a comparison. A thermogravimetric analyser coupled with a mass spectrometer (TG-MS) was used to examine the influence of catalyst loading, support material and the presence of additional water vapour on H<sub>2</sub> production and selectivity. Normalization of the raw MS data enabled semi-quantitative analysis of the product gas distribution, which facilitated reliable comparison between different experimental conditions. Catalysts were characterized by physisorption, chemisorption, TGA, XRD, SEM and TEM. SBA-15 and MCM-41 supported catalysts significantly elevated the yield and selectivity of H<sub>2</sub>, under dry Ar and with the injection of additional water vapour, when compared with the  $\gamma$ -Al<sub>2</sub>O<sub>3</sub> support. 15 wt.%Co/SBA-15 and 10 wt.%Co/MCM-41 were identified as the most active catalysts from the two groups with indicative yields of 202 and 303 ml H<sub>2</sub>/g cellulose, respectively. The 10 wt.%Co/MCM-41 catalyst gave with the highest H<sub>2</sub> selectivity reaching 21.7% of the dry product gas.

© 2010 Elsevier B.V. All rights reserved.

## 1. Introduction

Non-edible biomass is a renewable source of hydrogen (H<sub>2</sub>) that has attracted attention as a greenhouse-neutral energy carrier [1]. During gasification, the chain structure of lignocellulosic biomass is decomposed, with the evolved gas species undergoing secondary cracking and reforming reactions to yield a H<sub>2</sub>-rich product gas, non-degradable tars and char residues [2]. In addition, biomass gasification shows promise as being of sufficient scale to satisfy future demand [3–6]. However, for commercial applications, the production of H<sub>2</sub> from biomass requires further research to facilitate direct use of the hydrogen in fuel cells. For proton exchange membrane (PEM) fuel cells, H<sub>2</sub> is required at >99.9%.

The use of a catalyst has been investigated to enhance the H<sub>2</sub> yield from a wide range of feedstocks, including steam reforming of simple compounds like methanol [7,8], ethanol [9,10] and methane [11], as well as more complex fuels, e.g. bio-oils [12], coal [13] and biomass [14,15]. These catalytic processes usually involve cracking, steam reforming and water-gas shift reactions; for complex feedstocks the issue of tar cracking is prominent. Cracking and steam reforming reactions are typically endothermic and favor high gasification temperatures (>800 °C) whereas the water-gas shift reaction

is exothermic. Hence there is a tradeoff in terms of the gasification temperature that is optimal for promoting the decomposition of the higher-hydrocarbons (>C<sub>3</sub>) and the water-gas shift reaction [5,16]. With the use of selective catalysts, it becomes possible to degrade the tars and promote the reforming reactions at temperatures suitable for the water-gas shift reaction, generating a product gas consisting mainly of H<sub>2</sub> and CO<sub>2</sub> [17,18]. If CO<sub>2</sub> is removed from the system continuously, then the remaining H<sub>2</sub> is at a high concentration, theoretically >80% (dry) [19] with the possibility of direct use in a fuel cell.

Supported Ni and Co are two of the most common catalysts for reforming processes. In previous studies, Ni has been identified as one of the best metals for tar elimination by catalyzing C–C bond breakage; as well as being able to catalyze O–H and C–H bond cleavage [18,20–22]. Co is also active for C–C bond rupture and thus is able to catalyze the decomposition of tars and smaller molecules containing C and O [23]. The activity of Co in steam reforming reactions has also been investigated [15,24]. In addition, Co has been found to favor CO removal and promote the water-gas shift reaction [25,26], which is important for high-selectivity H<sub>2</sub> production from biomass.

We recently reported the influence of Ni on the product gas distribution and H<sub>2</sub> yield during biomass decomposition [27]. The application of a mesoporous silica support (MCM-41) significantly improved the performance compared with a  $\gamma$ -Al<sub>2</sub>O<sub>3</sub> support. Mesoporous materials such as MCM-41 and SBA-15 loaded with Co

\* Corresponding author. Tel.: +61 2 9351 2926.

E-mail address: [andrew.harris@sydney.edu.au](mailto:andrew.harris@sydney.edu.au) (A.T. Harris).

have previously been reported to provide good dispersion, stability and higher activity in specific reactions, e.g. selective oxidation of hydrocarbons [28] and benzene [25]. In this work we developed MCM-41 and SBA-15 supported Co catalysts to compare with previous research that showed Co/Al<sub>2</sub>O<sub>3</sub> gave higher selectivity to H<sub>2</sub> than Co/SiO<sub>2</sub>.  $\gamma$ -Al<sub>2</sub>O<sub>3</sub> supported Co is used as a reference material. We also continued the development of a TG-MS system to investigate catalyst activity, the influence of support materials, metal loading and the injection of additional H<sub>2</sub>O on the product gas yield and distribution. Finally, a comparison between Ni and Co in terms of activity, selectivity and coking-resistance is reported [29].

## 2. Experimental

### 2.1. Catalyst synthesis

SBA-15 was synthesized using a microwave-aging process with the addition of a block copolymer surfactant (Pluronic P123; PEO<sub>20</sub>PPO<sub>70</sub>PEO<sub>20</sub>) as a structure template [30]. Calcined SBA-15 and MCM-41 (Sigma–Aldrich) were used as catalyst supports. Both support materials were treated under vacuum at 383 K for 8 h to clean the pore surfaces prior to impregnation. We used a modified incipient wetness impregnation technique [27] to ensure even Co dispersion on the internal and external surfaces of the support materials. Co(NO<sub>3</sub>)<sub>2</sub>·6H<sub>2</sub>O (Sigma–Aldrich) was used as the Co precursor. Supported catalysts were prepared at 5, 10, 15 and 20 wt.% Co on  $\gamma$ -Al<sub>2</sub>O<sub>3</sub>, SBA-15 and MCM-41. Co oxides were reduced to metallic Co using two complementary techniques: (i) thermogravimetric (TG) reduction: samples were loaded into the TG apparatus, flushed with N<sub>2</sub> at 200 °C followed by reduction under 25 vol.% H<sub>2</sub> in N<sub>2</sub> by heating at 5 °C/min to 800 °C; (ii) chemisorption pretreatment reduction: samples were loaded into quartz U-tubes, evacuated, heated to 800 °C at 20 °C/min followed by introduction of H<sub>2</sub> at 800 °C for 1 h. Active catalysts (following reduction) were combined with methyl cellulose (Sigma–Aldrich, 99.9%) at a 1:1 mass-ratio using a high-speed vortex mixer and then stored under vacuum prior to use.

### 2.2. Catalyst characterization

N<sub>2</sub> adsorption and desorption isotherms, obtained at the temperature of liquid N<sub>2</sub> (Quantachrome Autosorb), were used to determine the BET surface area, total pore volume and pore size distribution (according to the BJH model). Thermogravimetric analysis (SDT Q600) was employed to investigate the reducibility of each as-synthesized catalyst using small quantities (~2 mg) of catalyst to minimize mass transfer effects.

H<sub>2</sub> chemisorption (Quantachrome Autosorb) was used to measure the active surface area of the catalysts and calculate the dispersion and average crystallite size of the supported Co. H<sub>2</sub> chemisorption was conducted at 75 °C with H<sub>2</sub> pressure increased from 40 to 820 mm Hg. The adsorption equilibration time was set at 30 min to approach full monolayer coverage [31]. The monolayer chemisorbed volume,  $V_m$ , was derived by extrapolation to  $P=0$  in isotherms of H<sub>2</sub> chemisorption. Based on the assumption of full monolayer coverage, the number of exposed Co sites was then calculated from  $V_m$ , enabling the estimation of the active surface area (ASA, m<sup>2</sup>/g), percent metal dispersion ( $D$ , %) and average crystallite size ( $d$ , nm) via Eqs. (1)–(3).

$$ASA = \frac{N_m S A_m}{166} \quad (1)$$

$$D = \frac{N_m S M}{100 L} \quad (2)$$

$$d = \frac{100 L f}{ASA \times Z} \quad (3)$$

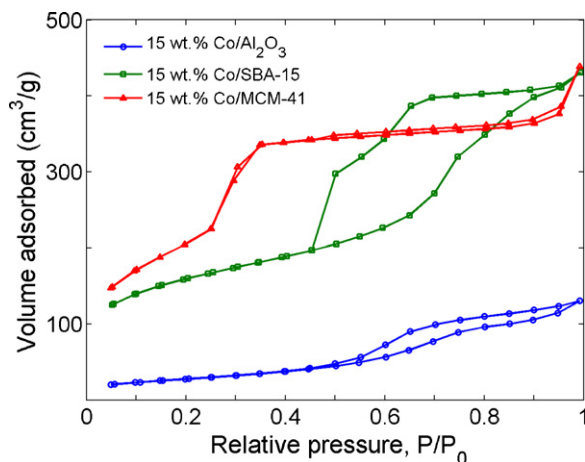


Fig. 1. N<sub>2</sub> adsorption/desorption isotherms for 15 wt.% Co on  $\gamma$ -Al<sub>2</sub>O<sub>3</sub>, SBA-15 and MCM-41.

$N_m$  ( $\mu$ mol/g) refers to the number of adsorbed gas molecules;  $S$  (=2 atoms/molecule) refers to the number of surface atoms covered by each chemisorbed gas molecule;  $A_m$  ( $\text{\AA}^2$ /atom) refers to the cross-sectional area occupied by each active surface atom; '166' in Eq. (1) is related to the units calculation;  $M$  refers to molecular weight of supported metal;  $L$  refers to percent loading of supported metal;  $f$  refers to particle shape correction factor (=6 for spherical particles).

The crystalline structure of the supported catalysts was assessed using powder diffraction (SIEMENS D5000 using Cu K $\alpha$  radiation,  $\lambda = 0.1542$  nm). Small-angle XRD patterns were measured from  $2\theta = 0.5^\circ$  to  $10^\circ$  with a step interval of  $0.01^\circ$ , while wide-angle patterns were measured between  $2\theta = 30^\circ$  and  $70^\circ$  with a step interval of  $0.02^\circ$ .

Scanning electron microscopy (FESEM, Zeiss Ultra+) was used to assess catalyst particle surface morphology and transmission electron microscopy (TEM, Philips CM120 BioFilter) was employed to gain insight into the inner pore structure and distribution of metal sites.

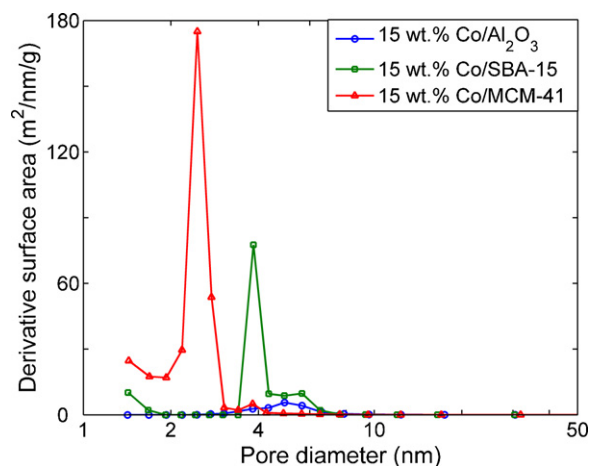
### 2.3. Determination of the catalyst activity

A modified TG-MS system with water vapour injection [27] was used, including semi-quantitative analysis of the product gas distribution, to assess the activity and selectivity of supported Co catalysts on the decomposition of cellulose. Well-mixed cellulose-catalyst samples were loaded into the TGA furnace and heated to 800 °C at a heating rate of 40 °C/min under a flow of dry or wet Ar. The signals of key ion fragments were recorded by MS and then normalized according to the method of Zhao et al. [27]. The generation rate and production of representative gas species could then be estimated. In this work we did not measure  $m/z = 45$  (C<sub>2</sub>H<sub>5</sub>O<sup>+</sup>) or  $m/z = 46$  (C<sub>2</sub>H<sub>5</sub>OH<sup>+</sup>) because their intensities were negligible compared with  $m/z = 31$  (CH<sub>2</sub>OH<sup>+</sup>).

## 3. Results and discussion

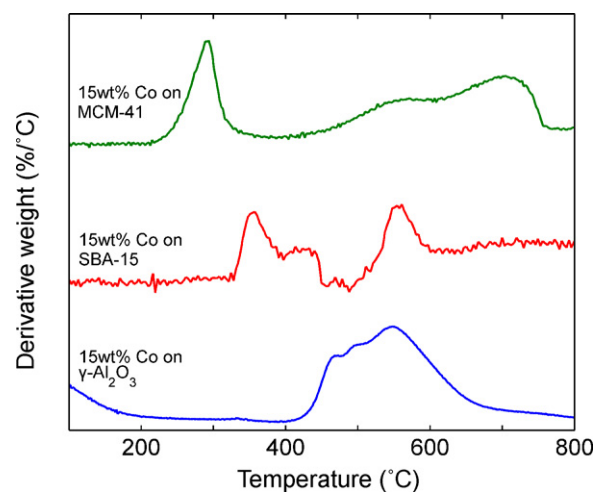
### 3.1. Catalyst characterization

Fig. 1 shows the adsorption/desorption isotherms of the three supported Co catalysts. Both SBA-15 and MCM-41 supported materials show typical type IV isotherms according to the BDDT classification, indicating the presence of meso-porosity [32]. The supported MCM-41 has a much narrower hysteresis loop with nearly parallel adsorption and desorption branches following the H1 type IUPAC classification and suggestive of a highly ordered



**Fig. 2.** Pore size distribution (BJH model, desorption data were used) for 15 wt.% Co on  $\gamma$ - $\text{Al}_2\text{O}_3$ , SBA-15 and MCM-41.

mesoporous structure with a narrow pore size distribution, as depicted in Fig. 2. The H2 type hysteresis behaviour of the SBA-15 supported catalyst implies that the pore size distribution and pore shape were not as well defined as the MCM-41 catalyst. For the  $\gamma$ - $\text{Al}_2\text{O}_3$  supported catalyst, the isotherm was type II, indicative of a non-porous (or macroporous) structure. However, slight



**Fig. 3.** Derivative weight loss in TG reduction (25 vol.%, 5 °C/min) for 15 wt.% Co on  $\gamma$ - $\text{Al}_2\text{O}_3$ , SBA-15 and MCM-41.

hysteresis between adsorption and desorption at high pressures is suggestive of the existence of some meso-pores. According to the pore size distribution analysed by the BJH model (Fig. 2), the MCM-41 supported catalyst showed the narrowest range of pores size, with the majority around 3 nm. The distribution of mesopores in

**Table 1**

Surface area ( $s$ :  $\text{m}^2/\text{g}$ , BET), pore volume ( $v$ :  $\text{cm}^3/\text{g}$ , BJH) and average pore size ( $d$ : nm, BJH) of supported Co catalysts.

		Blank support		5%Co		10%Co		15%Co		20%Co	
		$s$	$v$	$P^a$	$R^a$	$P^a$	$R^a$	$P^a$	$R^a$	$P^a$	$R^a$
$\gamma$ - $\text{Al}_2\text{O}_3$	$s$	155		121	117	116	110	109	101	102	95
	$v$	0.27		0.24	0.23	0.23	0.22	0.21	0.20	0.20	0.19
	$d$	8.0		8.0	8.1	8.1	8.2	8.1	8.0	8.2	8.1
SBA-15	$s$	830		703	654	623	585	599	553	535	493
	$v$	0.90		0.80	0.70	0.70	0.68	0.69	0.67	0.60	0.55
	$d$	4.3		4.6	4.7	4.6	4.7	4.9	4.8	4.9	4.8
MCM-41	$s$	979		905	859	865	815	798	759	684	617
	$v$	0.96		0.90	0.85	0.87	0.70	0.77	0.68	0.58	0.55
	$d$	3.9		3.8	3.7	3.7	3.6	3.6	3.6	3.6	3.6

<sup>a</sup> P—catalyst precursors, R—catalysts reduced using chemisorption pre-treatment (800 °C, pure  $\text{H}_2$ , 1 h).

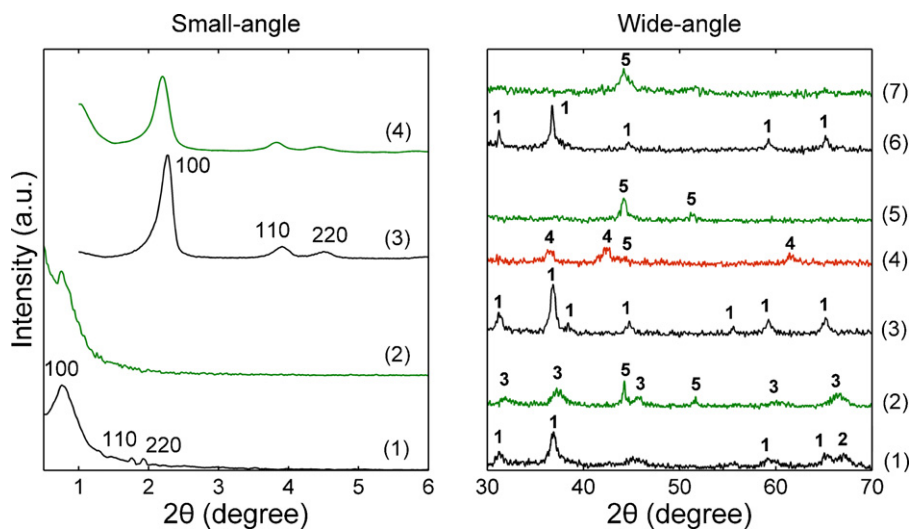


**Fig. 4.** Small-angle XRD patterns (left panel) for: (1) blank SBA-15, (2) reduced 15 wt.%Co/SBA-15, (3) blank MCM-41, and (4) reduced 15 wt.%Co/SBA-15; wide-angle patterns (right panel) for: (1) 15 wt.%Co/ $\gamma$ - $\text{Al}_2\text{O}_3$  (precursor), (2) 15 wt.%Co/ $\gamma$ - $\text{Al}_2\text{O}_3$  (reduced at 800 °C), (3) 15 wt.%Co/SBA-15 (precursor), (4) 15 wt.%Co/SBA-15 (reduced at 600 °C), (5) 15 wt.%Co/SBA-15 (reduced at 800 °C), (6) 15 wt.%Co/MCM-41 (precursor), and (7) 15 wt.%Co/MCM-41 (reduced at 800 °C). Five phases involved in patterns (1)–(7): 1,  $\text{Co}_3\text{O}_4$ ; 2,  $\text{Al}_2\text{O}_3$ ; 3,  $\text{Co}_2\text{AlO}_4/\text{CoAl}_2\text{O}_4$ ; 4,  $\text{CoO}$ ; 5,  $\text{Co}$  (0)

**Table 2**  
Reducibility of catalyst precursors.

	5%Co		10%Co		15%Co		20%Co	
Stoichiometric weight loss (Co <sub>3</sub> O <sub>4</sub> to Co)	1.78%		3.49%		5.14%		6.74%	
γ-Al <sub>2</sub> O <sub>3</sub>								
Major peaks (°C)	544		496		548		554	
Weight loss in TG (%)	1.5		3.2		4.9		6.2	
SBA-15								
Major peaks (°C)	275	719	289	705	293	707	310	722
Weight loss in TG (%)	0.4	2.1	1.0	3.8	1.7	4.8	2.9	5.0
MCM-41								
Major peaks (°C)	346	550	357	558	365	600	360	595
Weight loss in TG (%)	0.8	1.9	1.5	4.0	2.1	5.2	3.4	6.0

the SBA-15 catalyst was concentrated between 4 and 5 nm. The  $\gamma\text{-Al}_2\text{O}_3$  supported catalyst showed a much wider distribution of pore sizes.

The well-defined mesoporosity of the SBA-15 and MCM-41 supported catalysts enabled much higher BET surface areas (830 and 979  $\text{m}^2/\text{g}$ , respectively) than the  $\gamma\text{-Al}_2\text{O}_3$  support (155  $\text{m}^2/\text{g}$ ), and although the latter is one of the most popular catalyst support materials, its mesoporous structure provides a different allocation of active sites and thus pathways for mass transfer. Impregnation, calcination and higher-temperature reduction caused destruction in the structure of all three supports to a degree (Table 1). However, most of the surface area and pore volume was retained.

Fig. 3 shows the weight loss profiles of the three supported catalysts during reduction using the TG apparatus. Two differential weight loss peaks were observed for the SBA-15 and MCM-41 supported catalysts, while the  $\gamma\text{-Al}_2\text{O}_3$  supported catalyst exhibited a single, broad peak. The presence of two peaks is suggestive of a two stage reduction, attributable to the presence of an intermediate Co phase. This was confirmed by wide-angle XRD (Fig. 4, right panel).  $\text{Co}_3\text{O}_4$  (phase 1) was detected for all three groups of catalysts with an extra peak belonging to  $\text{Al}_2\text{O}_3$  (phase 2) also present in the pattern for Co on  $\gamma\text{-Al}_2\text{O}_3$  (pattern 1). After reduction in  $\text{H}_2$  at 800  $^\circ\text{C}$  for 1 h, only Co(0) (phase 5) was observed on 15 wt.%Co/SBA-15 (pattern 5) and 15 wt.%Co/MCM-41 (pattern 7). However, for the  $\text{Al}_2\text{O}_3$  supported catalysts (pattern 2) an additional phase was observed, most likely  $\text{Co}_2\text{AlO}_4/\text{CoAl}_2\text{O}_4$  (phase 3). Hence, under the conditions used, Co supported on SBA-15 and MCM-41 was completely reduced to its elemental state while Co supported on  $\gamma\text{-Al}_2\text{O}_3$  was only partially reduced. Therefore, the two weight loss peaks observed during reduction of SBA-15 and MCM-41 supported catalysts were probably attributed to two stage reduction:  $\text{Co}_3\text{O}_4$  to CoO and then CoO to Co, while the broad single peak for  $\gamma\text{-Al}_2\text{O}_3$  indicated a slow reduction of  $\text{Co}_3\text{O}_4$ , only part of which was reduced to Co(0). This conclusion is supported by the reducibility data given in Table 2. The overall weight loss for all catalysts supported on SBA-15 and MCM-41 was close to their stoichiometric value; but not for the  $\gamma\text{-Al}_2\text{O}_3$  group due to the formation of the stable 'spinel' structure ( $\text{CoAl}_2\text{O}_4/\text{Co}_2\text{AlO}_4$ ). The two-stage reduction for MCM-41 and SBA-41 supported catalysts was confirmed by the observation of CoO (phase 4) on 15 wt.%Co/SBA-15 reduced under  $\text{H}_2$  at 600  $^\circ\text{C}$  (pattern 4).

The left panel of Fig. 4 shows the small-angle XRD patterns for the mesoporous supports prior to and post-metal loading. The three main peaks (100), (110) and (220) are suggestive of a highly ordered structure with hexagonal symmetry [33] and were clearly observed for the patterns of blank SBA-15 and MCM-41 with different  $2\theta$  ranges (0.5–2 $^\circ$  and 2–5 $^\circ$ , respectively) indicative of meso-porosity with differing pore diameters. Slight changes in the intensity and position of these peaks were observed upon catalyst reduction for the 15 wt.%Co/MCM-41 (pattern 4), while the intensity of two of the peaks (110 and 220) were decreased for the

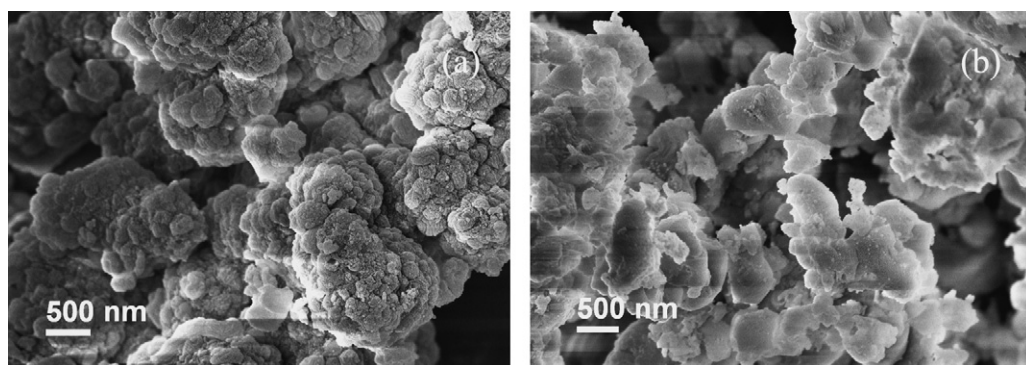
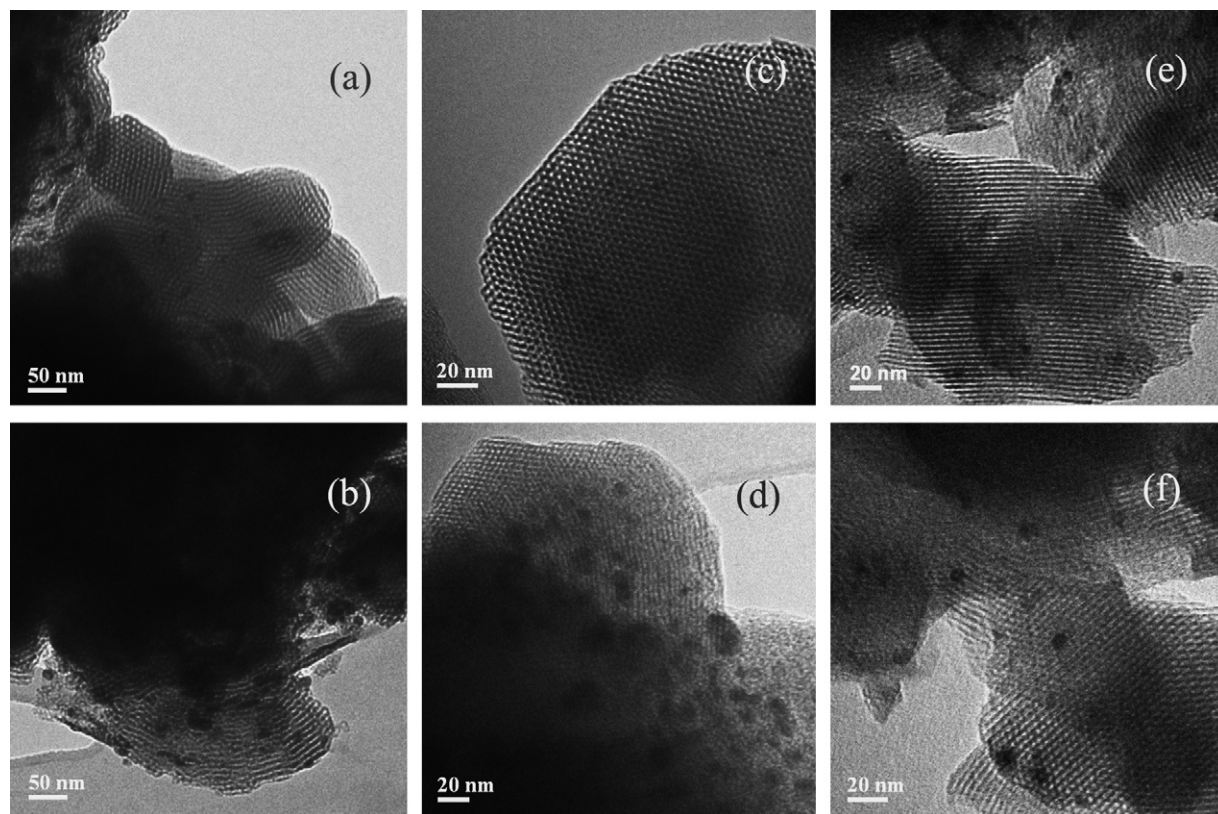
reduced 15 wt.%Co/SBA-15 (pattern 2) sample, implying that more mesoporosity was retained in the MCM-41 support than SBA-15 following impregnation, calcination and reduction.

$\text{H}_2$  chemisorption was used to determine the number of active Co sites present on each catalyst. For the mesoporous supported catalysts in this study, the dispersion of Co sites within the substrates is an essential factors influencing catalyst activity. The results based on Eqs. (1)–(3) has been listed in Table 3. The increase in metal loading did not result in a linear increase in the active surface area. 15 wt.%Co/ $\gamma\text{-Al}_2\text{O}_3$ , 15 wt.%Co/SBA-15 and 10 wt.%Co/MCM-41 exhibited the highest  $\text{H}_2$  uptake in each of the three groups, respectively, which is suggestive of a trade-off between increased metal loading and decreased metal dispersion. Despite having a lower BET surface area than 5 wt.%Co/MCM-41, 10 wt.%Co/MCM-41 showed a higher active metal surface area (14.2  $\text{m}^2/\text{g}$  for 5 wt.% increment of Co). However, the poor metal dispersion for 15 wt.%Co/MCM-41 (13.3%, much lower than the measured 21.0% for 10 wt.%Co/MCM-41) hindered further development of the active surface. For the SBA-15 group, the maximum number of active sites was measured for the 15 wt.% Co catalyst (10.7  $\text{m}^2/\text{g}$ ) due to the relatively large mean pore size (Fig. 2). However, this was still substantially lower than all of the MCM-41 supported catalysts. For  $\gamma\text{-Al}_2\text{O}_3$  group, the significantly lower BET surface area accommodated fewer active Co sites, resulting in poor Co dispersion (only 3.2% at most). Consequently, the active area for  $\gamma\text{-Al}_2\text{O}_3$  supported catalysts ( $\leq 2.1 \text{ m}^2/\text{g}$ ) was far below that of the two mesoporous supports.

Fig. 5 shows SEM images for (a) 15 wt.%Co/SBA-15 and (b) 15 wt.%Co/MCM-41, respectively. Both images confirm the porous morphology differs significantly from the  $\gamma\text{-Al}_2\text{O}_3$  supported catalysts. Although the catalysts had undergone high-temperature calcination and reduction, the SEM images show that each substrate was comparatively stable under these conditions. Fig. 6(a, b, e and f) shows TEM images of two different 15 wt.%Co/SBA-15 and 10 wt.%Co/MCM-41 catalysts, respectively. As a comparison, TEM images for 5 and 15 wt.%Co/MCM-41 are shown in (c) and (d). In all six images the ordered arrayed hexagonal porous structure is present. The TEM images in Fig. 6 provide information on the size and distribution of metal sites; these are consistent with the chemisorption calculations. For 10 wt.%Co/MCM-41, the Co particles range in size between 4 and 5 nm while for the 15 wt.%Co/SBA-15 they are  $\sim 10$  nm. Furthermore, 15 wt.%Co/SBA-15 showed a different allocation of Co particles: some small particles are observed in (Fig. 6a) while numerous larger particles are evident in (Fig. 6b), while 10 wt.%Co/MCM-41 displayed uniformly distributed metal sites with similar diameters (Fig. 6e and f). However, the images suggest that the 15 wt.%Co/MCM-41 (Fig. 6d) suffered from non-uniform metal dispersion due to the increased Co loading. For 5 wt.%Co/MCM-41 (c), fewer and finer Co particles were observed, which probably caused the lack of active surface area, despite them being evenly distributed.

**Table 3**Analysis results of H<sub>2</sub> chemisorption.

Co load (wt.%)	Monolayer chemisorbed volume, V <sub>m</sub> (ml/g, STP)	Active surface area (m <sup>2</sup> /g)	Percent metal dispersion (%)	Average crystallite size (nm)
$\gamma$ -Al <sub>2</sub> O <sub>3</sub>				
5	0.3	1.1	3.2	31.6
10	0.5	1.8	2.6	37.9
15	0.6	2.1	2.1	47.3
20	0.6	2.1	1.6	63.1
SBA-15				
5	2.1	7.5	22.1	4.5
10	2.6	9.2	13.7	7.3
15	3.0	10.7	10.5	9.5
20	2.9	10.3	7.6	13.1
MCM-41				
5	3.1	11.0	32.6	3.0
10	4.0	14.2	21.0	4.7
15	3.8	13.5	13.3	7.5
20	3.7	13.2	9.7	10.2

**Fig. 5.** Scanning electron micrographs for (a) 15 wt.%Co/SBA-15 and (b) 15 wt.%Co/MCM-41.**Fig. 6.** Transmission electron images of (a) and (b) 15 wt.%Co/SBA-15, (c) 5 wt.%Co/MCM-41, (d) 15 wt.%Co/MCM-41, and (e) and (f) 10 wt.%Co/MCM-41.

**Table 4**

Main reactions of catalytic biomass (cellulose) gasification.

Reaction	Equation	$\Delta H^\circ_{298.15}$ (kJ/mol)
Thermal decomposition	Biomass $\rightarrow$ H <sub>2</sub> O + CO + CO <sub>2</sub> + organicvolatiles + volatile tars + char (4)	–
Tars cracking (catalytic)	Tars $\rightarrow$ H <sub>2</sub> O + H <sub>2</sub> + CO + CO <sub>2</sub> + CH <sub>4</sub> + C <sub>x</sub> H <sub>y</sub> + CH <sub>3</sub> OH + CH <sub>2</sub> O + CH <sub>3</sub> CHO (5)	–
Catalytic cracking	CH <sub>3</sub> OH $\rightarrow$ CH <sub>2</sub> O + H <sub>2</sub> (6)	+85.0, endothermic
Catalytic cracking	CH <sub>2</sub> O $\rightarrow$ CO + H <sub>2</sub> (7)	+5.4, endothermic
Catalytic cracking	CH <sub>3</sub> CHO $\rightarrow$ CH <sub>4</sub> + CO (8)	–19.6, exothermic
Catalytic cracking/coking	CH <sub>4</sub> $\rightarrow$ C + 2H <sub>2</sub> (9)	+75, endothermic
Water-gas shift	CO + H <sub>2</sub> O $\rightarrow$ CO <sub>2</sub> + H <sub>2</sub> (10)	–41.1, exothermic
Steam reforming	CH <sub>4</sub> + H <sub>2</sub> O $\rightarrow$ CO + 3H <sub>2</sub> (11)	+206.2, endothermic
Steam reforming	C <sub>x</sub> H <sub>y</sub> + xH <sub>2</sub> O $\rightarrow$ xCO + (n + 0.5 m)H <sub>2</sub> (12)	Endothermic
Dry reforming	CH <sub>4</sub> + CO <sub>2</sub> $\rightarrow$ 2CO + H <sub>2</sub> (13)	+247.3, endothermic
Char gasification	C + CO <sub>2</sub> $\rightarrow$ 2CO (14)	+172.3, endothermic
Char gasification	C + 2H <sub>2</sub> O $\rightarrow$ CO <sub>2</sub> + 2H <sub>2</sub> (15)	+72.3, endothermic

### 3.2. Catalyst activity assessment using TG-MS

#### 3.2.1. H<sub>2</sub> generation from the decomposition of cellulose

As a glucose polymer, cellulose had been well studied as a model biomass compound, in particular the generation of a H<sub>2</sub>-rich gas via thermal decomposition. Due to the complexity of the reaction system, numerous mechanistic models have been proposed; however most of these are dependent upon which heterogeneous catalysts are present and the reaction system used [19,34–36]. We have previously proposed a model consisting of the main gas-phase reactions [27]. The key reactions are reported in Table 4.

During non-catalyzed decomposition of biomass, the reactions will most likely stop at the thermal decomposition of tars (Eq. (5)). However, utilization of an active catalyst can promote the further cracking of tars and trigger the remaining reactions listed in Table 4. Smaller fragments are further cracked into CO, CH<sub>4</sub> and C in addition to H<sub>2</sub> (Eqs. (6)–(9)), and the introduction of H<sub>2</sub>O enables reforming of these unwanted intermediates into H<sub>2</sub> and CO<sub>2</sub> (Eqs. (10)–(15)). Thus a good catalyst with high activity and selectivity for these cracking and reforming reactions will enhance the production and purity of H<sub>2</sub> in the product gas during biomass decomposition. Fig. 7 compares the influence of the three groups of Co catalysts on the cumulative H<sub>2</sub> yields measured during pyrolytic decomposition of cellulose from 200 to 600 °C in Ar, with and without additional water vapour introduced (1 vol.% in total carrier gas). The methods

of normalization of the raw data were described previously [27]. Table 5 lists the char yield (wt.% of cellulose) at 600 °C, total dry gas yields and H<sub>2</sub>O yield.

In the absence of a catalyst, the total dry gas yield was 719 ml/g (Table 5), consisting of 1.5 vol.% H<sub>2</sub>, presumably derived solely from thermal decomposition of the cellulose. The presence of the blank support (Al<sub>2</sub>O<sub>3</sub> and SiO<sub>2</sub>) resulted in a slight increase in H<sub>2</sub> and total gas yields (Fig. 7 and Table 5), while a significant increase in both was observed when Co was present.  $\gamma$ -Al<sub>2</sub>O<sub>3</sub> is a solid acid catalyst [37] while SBA-15 and MCM-41 also possess mild acidic sites on their respective surfaces [38]. Hence the slight increase in H<sub>2</sub> yield for the experiment in the presence of the blank supports is likely attributable to enhancement of the cracking reactions of large molecules (mainly Eq. (5) in Table 4). The substantial increase in total gas yield (up to 65 vol.% in dry Ar, Table 5) confirmed the activity of Co for cracking tars and small fragments derived during thermal decomposition (Eq. (5)–(9)). The significant increase in H<sub>2</sub> yield (from ~10 ml/g to >300 ml/g, Fig. 7) is ascribed to the promotion of the reforming reactions, e.g. water-gas-shift (Eq. (10)), steam and dry reforming (Eqs. (11)–(13)).

Although the improved gas yield is mainly attributable to the presence of Co, the substrate materials also play an important role in modifying catalyst activity. During decomposition, without additional water vapour, the maximum H<sub>2</sub> output (84.1 ml/g, Fig. 7) was observed with 15 wt.% Co for  $\gamma$ -Al<sub>2</sub>O<sub>3</sub> group. The same Co loading

**Table 5**Yields of char, H<sub>2</sub>O and total dry gas for cellulose pyrolysis in dry and wet Ar.

	Char yield at 600 °C (wt.%)		H <sub>2</sub> O yield (ml/g cellulose)		Total dry gas yields (ml/g cellulose)	
	In dry Ar	In wet Ar	In dry Ar	In wet Ar	In dry Ar	In wet Ar
No catalyst	13.5	12.8	515.2	589.3	718.8	797.4
$\gamma$ -Al <sub>2</sub> O <sub>3</sub>						
0	12.2	– <sup>a</sup>	594.1	–	767.5	–
5 wt.%	15.1	–	483.0	–	785.0	–
10 wt.%	12.4	–	551.1	–	928.9	–
15 wt.%	12.9	–	579.2	–	942.8	–
20 wt.%	13.1	–	559.0	–	936.2	–
SBA-15						
0	17.1	16.1	624.5	752.9	746.2	827.8
5 wt.%	13.0	12.4	772.2	848.7	1159.4	1249.4
10 wt.%	12.3	11.0	808.5	778.1	1213.1	1364.3
15 wt.%	11.7	11.4	646.1	785.5	1159.4	1286.6
20 wt.%	13.0	12.8	645.4	668.0	1165.9	1287.6
MCM-41						
0	14.3	12.9	707.7	935.1	897.7	1014.8
5 wt.%	12.9	11.3	522.4	801.6	1167.0	1411.3
10 wt.%	11.1	10.1	518.0	546.9	1138.7	1396.0
15 wt.%	13.7	12.5	488.3	656.0	1156.4	1379.5
20 wt.%	14.0	13.2	543.6	711.1	1185.4	1364.9
5 wt.%Ni/MCM-41	13.4	10.7	586.9	780.5	1189.2	1371.8

<sup>a</sup> TG-MS test with  $\gamma$ -Al<sub>2</sub>O<sub>3</sub> supported catalysts in wet Ar was not conducted.

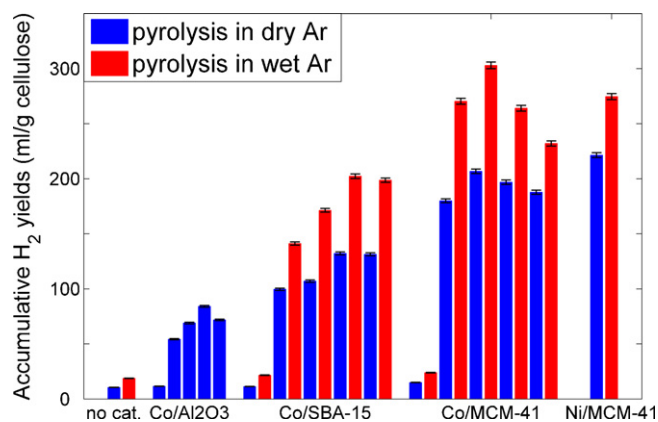


**Fig. 7.** Accumulative  $H_2$  yields for cellulose decomposition in dry and wet Ar (200–600 °C). The five pairs of columns corresponding Co/SBA-15 refer to 0 wt.%, 5 wt.%, 10 wt.%, 15 wt.% and 20 wt.% Co/SBA-15, respectively. The five pairs of columns corresponding Co/MCM-41 refer to 0 wt.%, 5 wt.%, 10 wt.%, 15 wt.% and 20 wt.% Co/MCM-41, respectively. The single pair of columns corresponding Ni/MCM-41 refer to 5 wt.% Ni/MCM-41.

**Table 6**

Maximum rate point for decomposition or generation rate<sup>a</sup> (°C).

	Cellulose	$H_2O$	$CO_2$	CO	$H_2$
No catalyst	378	373	374	378	381
15 wt.%Co/ $\gamma$ - $Al_2O_3$	371	374	374	376	374
15 wt.%Co/SBA-15	374	374	374	378	387
10 wt.%Co/MCM-41	376	373	377	381	388

<sup>a</sup> Decomposition rate of cellulose was measured by DTG curve, and generation rate of  $H_2O$ ,  $CO_2$ , CO and  $H_2$  was measured by normalized MS signals.

on the SBA-15 support increased this significantly to 132.3 ml/g, while the MCM-41 supported Co performed even better (206.8 ml/g for 10 wt.% Co).  $H_2$  yield is consistent with the active surface area measured by  $H_2$  chemisorption confirming that the important heterogeneous reactions depend strongly on the dispersion and area of active sites. A substantial increase in  $H_2$  output and the total gas yield were observed with the introduction of additional water vapour. This is discussed in Section 3.2.3.

The data in Fig. 8 show how the three groups of catalysts influence the kinetics of cellulose decomposition in terms of the rate of generation of  $H_2$  ( $m/e=2$ , left panel) and derivative weight loss of the cellulose (right panel). The derivative weight loss peaks indicate that nearly all product gas species were evolved during heating between 200 and 600 °C. Fig. 9 compares the different rates of production of  $H_2O$ ,  $CO_2$ , CO and  $H_2$  with 10 wt.%Co/MCM-41, and Table 6 lists the temperature at which the rate of decomposition of cellulose is at a maximum and the generation of these four species with no catalyst, 15 wt.%Co/ $\gamma$ - $Al_2O_3$ , 15 wt.%Co/SBA-15

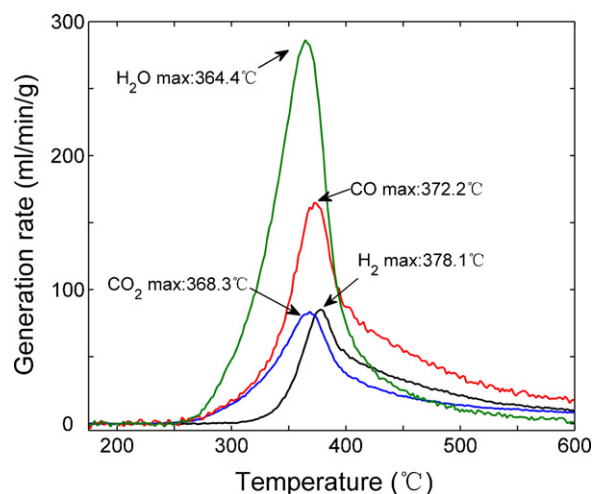


**Fig. 9.** Comparison of kinetics between  $H_2O$ ,  $CO_2$ , CO and  $H_2$  for 10 wt.%Co/MCM-41.

and 10 wt.%Co/MCM-41, respectively.  $H_2$  generation commenced ~50 °C later than the commencement of decomposition and continued after decomposition was complete with a lag in the tail of the primary peak (Fig. 8). In contrast, the evolution of  $H_2O$ ,  $CO_2$  and CO was consistent with the decomposition of cellulose (Fig. 8, right panel; Fig. 9 and Table 6). This result confirms the priority of Eqs. (4) and (5), and the endothermicity of most of the remaining reactions in Table 4. The enhancement was observed on the generation rate of  $H_2$  (Fig. 8, left panel) by the mesoporous catalysts. Although 15 wt.%Co/ $\gamma$ - $Al_2O_3$  enhanced the maximum rate of production of  $H_2$ , SBA-15 and MCM-41 supported Co were two and three times more effective at generating  $H_2$ , respectively.

### 3.2.2. $H_2$ selectivity of catalysts

Fig. 10 shows how the three groups of catalysts influence the distribution (vol.%) of species evolved from the dry decomposition of cellulose. All the blank supports exhibited almost no effect on  $H_2$  concentration and only slight adjustment for other species, e.g.  $CO_2$  and  $CH_3OH$ , confirming their limited activity for the reforming reactions. However, for the supported Co catalysts, selectivity towards  $H_2$  and CO was significantly increased, with a subsequent decline for all other major species. This further confirms the activity of Co for the cracking and reforming reactions in Table 4. The substantial decrease in char yield at 600 °C (Table 6) also demonstrates the anti-coking ability of Co, attributable to enhancement of the char gasification reactions (Eqs. (14) and (15)).

15 wt.%Co/ $\gamma$ - $Al_2O_3$ , 15 wt.%Co/SBA-15 and 10 wt.%Co/MCM-41 showed the best  $H_2$  selectivity amongst the three groups of catalysts (8.9, 11.4 and 18.2 vol.%, respectively), and correspondingly

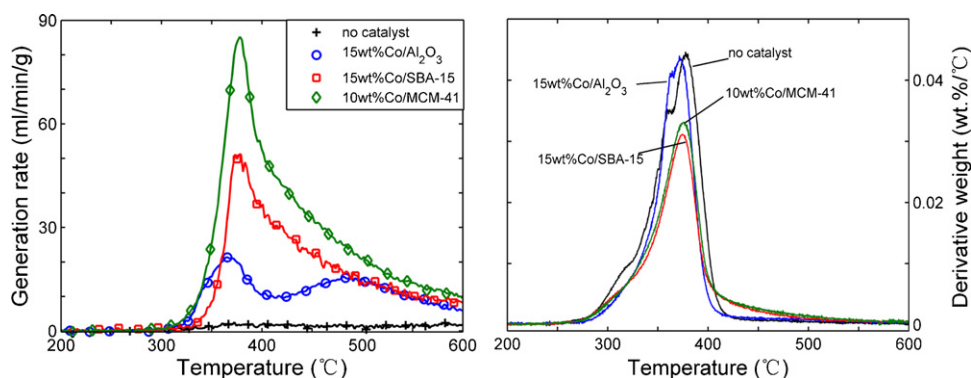


**Fig. 8.** Influence of catalysts on  $H_2$  generation rate (left panel) and decomposition weight loss profile (right panel) during decomposition in dry Ar.

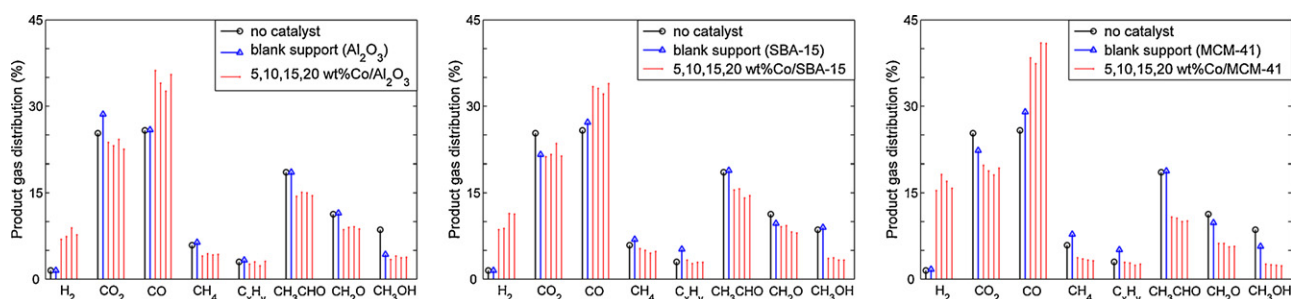


Fig. 10. Influence of catalysts on distribution of gaseous species evolved during the cellulose decomposition.

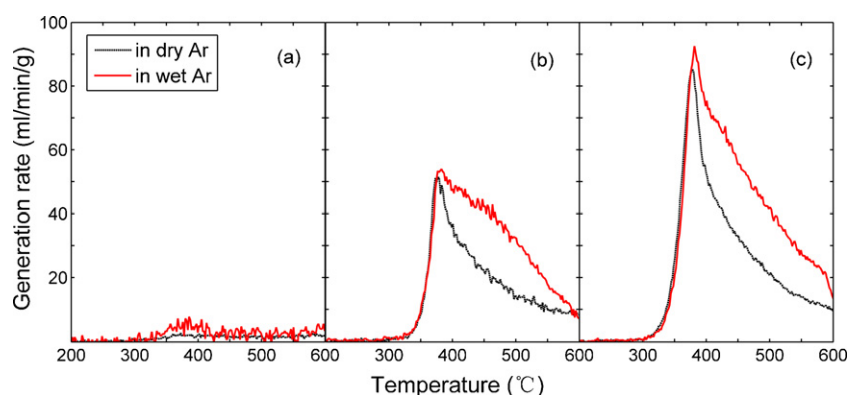


Fig. 11. Influence of additional H<sub>2</sub>O on H<sub>2</sub> generation rate with (a) no catalyst, (b) 15 wt.%Co/MCM-41, and (c) 10 wt.%Co/MCM-41.

the lowest CO (Fig. 10) and H<sub>2</sub>O concentrations (Table 5) indicating the largest consumption of CO and H<sub>2</sub>O. These results provide evidence of the activity of Co for the water-gas-shift reaction and are consistent with previous studies showing the ability of Co for removing CO [25,26]. However, MCM-41 supported Co showed higher CO selectivity than the other two groups, which can be ascribed to higher activity towards the cracking reactions. Of the MCM-41 supported catalysts, the 10 wt.%Co/MCM-41 catalyst was optimum for the dry decomposition of cellulose, with the yields of CO<sub>2</sub>, CH<sub>4</sub>, CH<sub>3</sub>CHO, CH<sub>2</sub>O and CH<sub>3</sub>OH all lower than for the 15 wt.%Co/ $\gamma$ -Al<sub>2</sub>O<sub>3</sub> and 15 wt.%Co/SBA-15 catalysts.

### 3.2.3. Influence of additional water vapour

Fig. 11 shows how the presence of a small quantity of additional water vapour influenced the generation rate of H<sub>2</sub>. The presence of extra H<sub>2</sub>O started to change the kinetics when the maximum reaction rate was reached, by prolonging the generation reactions beyond 380 °C and consequently increasing the total production of H<sub>2</sub>. The enhancement is likely attributable to the promotion of the endothermic steam reforming reactions (Eqs. (11) and (12))

and the water-gas-shift reaction. According to Fig. 7, introduction of H<sub>2</sub>O (1 vol.%) caused ~50% elevation in H<sub>2</sub> yield with mesoporous supported Co catalysts, reaching 202 ml/g and 303 ml/g for 15 wt.%Co/SBA-15 and 10 wt.%Co/MCM-41, respectively. However, only a 25% increase in H<sub>2</sub> yield (from 221 to 275 ml/g) was observed for 5 wt.%Ni/MCM-41 [27]. Furthermore, MCM-41 supported Co gave lower apparent char yields (at 600 °C) and H<sub>2</sub>O output than for Ni supported catalysts (Table 6). These results suggested that Co is more active for the water-gas-shift reaction than Ni.

The presence of additional H<sub>2</sub>O also tuned the distribution of the evolved gaseous products as shown in Fig. 12. The influence of additional H<sub>2</sub>O in the feed was negligible when no catalyst was present but significant with mesoporous supported Co. The most remarkable change was observed for 10 wt.%Co/MCM-41, where the introduction of 1 vol.% H<sub>2</sub>O increased the H<sub>2</sub> selectivity by ~20 vol.% (reached 21.7% in dry product gas) and correspondingly decreased the value of CO by ~13 vol.%. These two parameters were just 7.5 and 7.4 vol.%, respectively for a 5 wt.%Ni/MCM-41, which again suggests that Co is more active for CO removal via the water-gas-shift reaction.

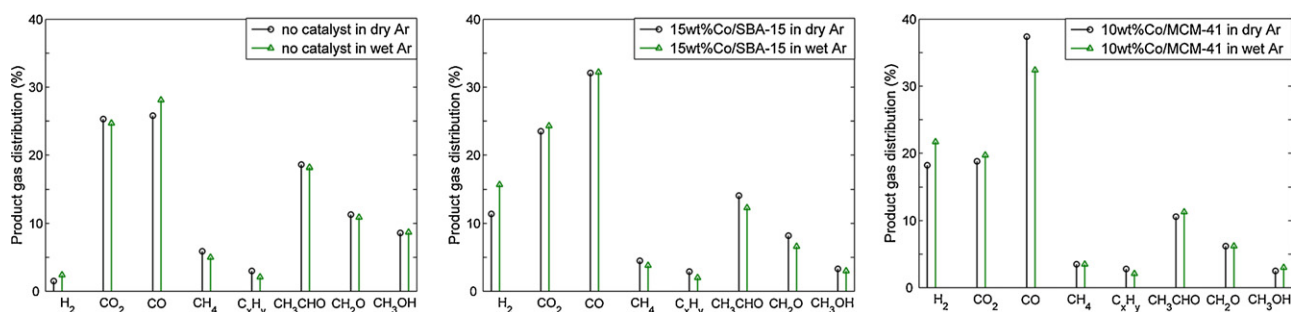


Fig. 12. Influence of additional water vapour (1 vol.%) on the product gas distribution.

#### 4. Conclusions

Mesoporous supported Co catalysts were developed using an incipient wetness impregnation technique. The consistent pore structure of MCM-41 and SBA-15 was superior in obtaining a uniform distribution of Co particles that were regular in shape with a narrow size distribution. There was a trade-off between metal loading and dispersion that ultimately limited the maximum active surface area, in direct proportion to the activity of supported Co catalyst. 10 wt.%Co/MCM-41 and 15 wt.%Co/SBA-15 were identified as the best catalysts of the two groups, respectively, with indicative yields of 202 and 303 ml H<sub>2</sub>/g cellulose, respectively. The 10 wt.%Co/MCM-41 catalyst gave with the highest H<sub>2</sub> selectivity reaching 21.7% of the dry product gas.

#### Acknowledgements

MZ is grateful to the Chinese Scholarship Council and the University of Sydney for a postgraduate scholarship. This work was funded, in part, by the Australian Research Council under DP0666488.

#### References

- [1] M. Balat, M. Balat, *Int. J. Hydrogen Energy* 34 (2009) 3589–3603.
- [2] P. McKendry, *Bioresour. Technol.* 83 (2002) 37–46.
- [3] P. McKendry, *Bioresour. Technol.* 83 (2002) 47–54.
- [4] M. Asadullah, *Appl. Catal. A: Gen.* 255 (2003) 169–180.
- [5] N.H. Florin, A.T. Harris, *Int. J. Hydrogen Energy* 32 (2007) 4119–4134.
- [6] N.H. Florin, A.T. Harris, *Chem. Eng. Sci.* 63 (2008) 287–316.
- [7] R. Pérez-Hernández, G. Mondragón Galicia, D. Mendoza Anaya, J. Palacios, C. Angeles-Chavez, J. Arenas-Alatorre, *Int. J. Hydrogen Energy* 33 (2008) 4569–4576.
- [8] X. Deng, J. Sun, S. Yu, J. Xi, W. Zhu, X. Qiu, *Int. J. Hydrogen Energy* 33 (2008) 1008–1013.
- [9] T.D. Ekin Ozdogan, G. Dogu, *Int. J. Chem. React. Eng.* 5 (2007).
- [10] M.A. Goula, S.K. Kontou, P.E. Tsiakaras, *Appl. Catal. B: Environ.* 49 (2004) 135–144.
- [11] F. Pompeo, D. Gazzoli, N.N. Nichio, *Int. J. Hydrogen Energy* 34 (2009) 2260–2268.
- [12] L.P.R. Profeti, E.A. Ticianelli, E.M. Assaf, *Int. J. Hydrogen Energy* 34 (2009) 5049–5060.
- [13] R.C. Timpe, R.W. Kulas, W.B. Hauserman, R.K. Sharma, E.S. Olson, W.G. Willson, *Int. J. Hydrogen Energy* 22 (1997) 487–492.
- [14] E.F. Iliopoulou, E.V. Antonakou, S.A. Karakoulia, I.A. Vasalos, A.A. Lappas, K.S. Triantafyllidis, *Chem. Eng. J.* 134 (2007) 51–57.
- [15] T. Furusawa, A. Tsutsumi, *Appl. Catal. A: Gen.* 278 (2005) 195–205.
- [16] E. Ozdogan, T. Dogu, G. Dogu, *Int. J. Chem. React. Eng.* 5 (2007).
- [17] T. Hanaoka, T. Yoshida, S. Fujimoto, K. Kamei, M. Harada, Y. Suzuki, H. Hatano, S.-y. Yokoyama, T. Minowa, *Biomass Bioenergy* 28 (2005) 63–68.
- [18] D. Sutton, B. Kelleher, J.R.H. Ross, *Fuel Process. Technol.* 73 (2001) 155–173.
- [19] N.H. Florin, A.T. Harris, *AIChE J.* 54 (2008) 1096–1109.
- [20] J. Han, H. Kim, *Renew. Sust. Energy Rev.* 12 (2008) 397–416.
- [21] D.C. Grenoble, M.M. Estadt, D.F. Ollis, *J. Catal.* 67 (1981) 90–102.
- [22] R.R. Davda, J.W. Shabaker, G.W. Huber, R.D. Cortright, J.A. Dumesic, *Appl. Catal. B: Environ.* 56 (2005) 171–186.
- [23] M. Ni, D.Y.C. Leung, M.K.H. Leung, K. Sumathy, *Fuel Process. Technol.* 87 (2006) 461–472.
- [24] A.F. Lucedio, E.M. Assaf, *J. Power Sources* 159 (2006) 667–672.
- [25] Z. Mu, J.J. Li, H. Tian, Z.P. Hao, S.Z. Qiao, *Mater. Res. Bull.* 43 (2008) 2599–2606.
- [26] G. Marbán, I. López, T. Valdés-Solís, A.B. Fuertes, *Int. J. Hydrogen Energy* 33 (2008) 6687–6695.
- [27] M. Zhao, N.H. Florin, A.T. Harris, *Appl. Catal. B: Environ.* 92 (2009) 185–193.
- [28] S. Todorova, V. Pârvulescu, G. Kadinov, K. Tenchev, S. Somacescu, B.L. Su, *Micro-porous Mesoporous Mater.* 113 (2008) 22–30.
- [29] J. Xu, W. Zhou, Z. Li, J. Wang, J. Ma, *Int. J. Hydrogen Energy* 34 (2009) 6646–6654.
- [30] A.T. Harris, A.R. Maddocks, R.J. Braham, *Asia Pacific Journal of Chemical Engineering*, in press, doi:10.1002/apj.360.
- [31] X. Shen, L.-J. Garces, Y. Ding, K. Laubernds, R.P. Zerger, M. Aindow, E.J. Neth, S.L. Suib, *Appl. Catal. A: Gen.* 335 (2008) 187–195.
- [32] K.S.W. Sing, D.H. Everett, R.A.W. Haul, L. Moscou, R.A. Pierotti, J. Rouquerol, T. Siemieniowska, *Pure Appl. Chem.* 57 (1985) 603.
- [33] D. Zhao, J. Feng, Q. Huo, N. Melosh, G.H. Fredrickson, B.F. Chmelka, G.D. Stucky, *Science* 279 (1998) 548–552.
- [34] M.J. Antal Jr., G. Varhegyi, *Ind. Eng. Chem. Res.* 34 (1995) 703–717.
- [35] H. Yang, R. Yan, H. Chen, D.H. Lee, C. Zheng, *Fuel* 86 (2007) 1781–1788.
- [36] G. Varhegyi, M.J. Antal, T. Szekeley, F. Till, E. Jakab, *Energy Fuels* 2 (1988) 267–272.
- [37] J. Li, R. Yan, B. Xiao, D.T. Liang, L. Du, *Environ. Sci. Technol.* 42 (2008) 6224–6229.
- [38] A. Corma, *Chem. Rev.* 97 (1997) 2373–2420.